Journal of Rock Mechanics and Geotechnical Engineering 18 (2026) 3483–3498

Contents lists available at ScienceDirect

Journal of Rock Mechanics and Geotechnical Engineering

journal homepage: www.jrmge.cn

Full Length Article

Identification of coal-rock interface under uniaxial compression using electric potential method

Tiancheng Shan [a,b,c], Zhonghui Li [a,b,c,*], Enyuan Wang [a,b,c], Haishan Jia [a,b,c], Xin Zhang [a,b,c], Qiming Zhang [a,b,c], Xiaoran Wang [a,d], Yue Niu [a,e], Shishi Deng [a,b,c]

[a] Key Laboratory of Coal Mine Gas and Fire Prevention and Control of the Ministry of Education, China University of Mining and Technology, Xuzhou, 221116, China
[b] National Engineering Research Center for Coal Gas Control, China University of Mining and Technology, Xuzhou, 221116, China
[c] School of Safety Engineering, China University of Mining and Technology, Xuzhou, 221116, China
[d] State Key Laboratory of Coal Resources and Safe Mining, China University of Mining and Technology, Xuzhou, 221116, China
[e] State Key Laboratory for GeoMechanics and Deep Underground Engineering, China University of Mining and Technology, Xuzhou, 221116, China

ARTICLE INFO

Article history:
Received 27 January 2025
Received in revised form
26 August 2025
Accepted 27 August 2025
Available online 14 January 2026

Keywords:
Coal-rock samples
Electric potential method
Mechanical response feature
Spatial distribution imaging
Interface identification
Uniaxial compressive failure

ABSTRACT

The instability of composite coal-rock structures can easily trigger severe dynamic disasters, such as rockbursts. The application of electric potential (EP) method shows promise for disaster prediction and accurate identification of coal-rock interfaces. In this study, uniaxial compression experiments were conducted to monitor the EP spatiotemporal response of fine sandstone-coal and coarse sandstone-coal combined samples. EP distribution contour maps and three-dimensional (3D) EP models were utilized to explore the failure mechanisms and identify the interface state. Then the relationship between EP response and force field was examined through numerical simulations. An EP-based multifractal method was utilized to predict rock failure. Results show that the intensity and polarity of EPs differ between coal and rock but are correlated with stress state. The progressive failure features of two types of combined samples differ, triggering distinct EP responses. In the EP contour maps, the EP level increases with increasing height, and a low-intensity signal band appears around the interface before failure. When failure occurs, the EP field changes, and the low-intensity signal band becomes distorted. The 3D EP models effectively visualize the progressive failure of combined samples and clearly identify the interface location, similar to acoustic emission (AE) location. The evolution of force chain field is closely related to EP generation, and sparse strong force chain fields leads to a significant increase in EP level. Furthermore, the EPs display multifractal features, with precursory information being reflected in $\Delta\alpha$ and Δf. This study provides new ideas for early-warning of composite coal-rock and coal-rock interface identification.

1. Introduction

The extraction of deep resources and the utilization of underground space predominantly occur within multilayered rock formations, making their consideration critical in engineering design and tunnel stability assessments (Rutqvist et al., 2008; Wang et al., 2022). With the gradual depletion of shallow resources in China, coal mining and underground space development are progressively advancing into deep zones exceeding 1000 m (He et al., 2018; Jiang et al., 2024). Meanwhile, under complex conditions of deep mining disturbances, coal-rock dynamic disasters such as rockbursts and coal-gas outbursts have increased in severity, posing significant threats to the safe and efficient extraction of coal resources, and the stable operation of underground spaces (Xie et al., 2019). For example, a rockburst event at the Hongyang No. 3 Mine in Shenyang, China caused severe casualties and property damage. This incident occurred at a longwall face with a mining depth of 1082 m, where vertical disturbances caused by roof failure acted on the coal-rock blocks. The vibrations weakened the friction between the coal seam and the roof and floor, leading to a sliding displacement of approximately 3 m of the coal pillar

* Corresponding author. Key Laboratory of Coal Mine Gas and Fire Prevention and Control of the Ministry of Education, China University of Mining and Technology, Xuzhou, 221116, China.
E-mail address: leezhonghui@163.com (Z. Li).

Peer review under responsibility of Institute of Rock and Soil Mechanics, Chinese Academy of Sciences.

https://doi.org/10.1016/j.jrmge.2025.08.052

(Li et al., 2024a). Fundamentally, these disasters result from the overall instability and failure of coal-rock composite systems, which are composed of coal seams and overlying rock strata. This process involves complex interactions between rock layers of different lithologies, making the failure mechanisms substantially more intricate than those of a single coal or rock layer (Li et al., 2024b). Moreover, the coal-rock interface is recognized as the weakest link in the coal-rock composite system and often acts as a stress concentration zone (Haeri et al., 2019). The accurate identification of coal-rock interface is necessary for delineating coal seam boundaries and optimizing support design. Therefore, studying the instability and disaster mechanisms of coal-rock composite systems can provide valuable insights into coal mining and underground space design and a basis for identifying transitions and boundaries within coal-rock layers.

In recent years, numerous scholars have conducted detailed investigations into the mechanical properties and deformation instability characteristics of coal-rock bodies, utilizing extensive laboratory experiments and numerical simulations (Zhang et al., 2020; Fu et al., 2022; Ma et al., 2022). Research findings indicate that owing to the strength differences between coal and rock bodies, the failure mechanisms of combined coal-rock bodies differ significantly from those of single coal or rock bodies, which exhibit progressive failure characteristics caused by the interfacial constraint effect (Liu et al., 2018; Shan et al., 2024a). By establishing damage constitutive models based on a series of connections of Newtonian bodies, which achieve a fitting optimization of more than 0.95 with actual mechanical curves, the mechanical behaviors of coal-rock composites with various combination types can be effectively described (Liu et al., 2018). Furthermore, coal often displays weaker mechanical properties in the coal-rock composite systems, which directly affects the overall stability of the system (Zuo et al., 2013). Previous studies have analyzed the factors influencing the failure behaviors and mechanical properties of combined coal-rock bodies, including the combination pattern (Li et al., 2022), rock strength (Cai et al., 2024), coal-rock height ratio (Yang et al., 2022), interface inclination angle (Cheng et al., 2020a), and interface cohesion characteristics (Zhao et al., 2015). For example, as the coal-rock height ratio and interface inclination angle increase, the mechanical properties of combined coal-rock samples weaken, making them more prone to failure. The combined coal-rock samples are typically used to assess the impact tendencies of coal-rock systems and provide important references for coal mine operations. Compared with single coal or rock masses, the coal-rock bodies offers a more realistic representation of the mechanical behaviors and instability mechanisms observed in coal-rock systems at mining sites (Xu et al., 2024; Lu et al., 2025). Moreover, the identification of coal-rock interface conditions has received significant attention in the field, such as mining design, construction safety, resource exploration, and dynamic disaster prevention. Furthermore, the stability of the coal-rock composite system is closely related to the mechanical behaviors of rocks and discrete element particles. A novel composite foundation system, known as the caliche stiffened pile, has been proposed, and its significant advantages in terms of optimizing pile length, controlling settlement, and enhancing foundation bearing capacity have been demonstrated through finite element analysis and parametric studies, which may reduce settlement by a maximum of 50 % (Stone et al., 2023). In the coal-rock composite system, the coal pillars undergo progressive deformation during cyclic loading and unloading, potentially losing their supporting capacity and leading to roof subsidence. Reinforcing measures, such as geogrid strengthening, can help reduce coal pillar failure and effectively enhance the stability of a foundation system (Farhangi et al., 2023; Li et al., 2024b). Several studies have used numerical simulations to reveal the impact of particle contact forces, stress transfer mechanisms, and friction behavior on the mechanical features of discrete element particles and have contributed to the understanding of coal-rock failure evolution (Farhangi et al., 2024; Jing et al., 2024). To date, techniques such as core drilling and three-dimensional (3D) laser scanning are widely used to accurately delineate interface positions, and monitoring methods such as microseismic monitoring and electrical detection have been applied in this domain.

The failure process of coal-rock combination bodies involves the nucleation, development, and propagation of microcracks (Fu et al., 2024), which are often accompanied by the generation of various geophysical signals, including acoustic emission (AE) (Dong et al., 2022), electromagnetic radiation (Li et al., 2023), infrared radiation (Yao et al., 2020), and EP (Shan et al., 2024b). In recent years, AE technology has been widely applied for monitoring and analyzing the damage evolution of combined coal-rock. This technology can effectively capture the occurrence of microcracking and is a valuable tool for accurately investigating the failure process of rocks (Liu et al., 2020). AE temporal parameters, including the hit, energy, amplitude and dominant frequency, are capable of reflecting the deformation characteristics of rocks (Archer et al., 2016; Yi et al., 2024). In addition, AE event localization provides insight into internal crack propagation within rocks (Xiao et al., 2017). There are significant differences in the local fracture behaviors of coal and rock bodies under interface confinement, leading to distinct variations in the temporal response and spectral evolution of the AEs at different locations (Huang and Liu, 2013; Song et al., 2021). AE analysis can also be used to investigate the tensile-shear failure characteristics at the rock-concrete interface (Shams et al., 2024). However, using exciting monitoring methods to monitor rock failure may lead to loss of critical information and inaccurate prediction timing. Therefore, incorporating EP monitoring in combined coal-rock failure offers a promising approach for supplementing and improving the understanding of rock fracturing behavior, providing more comprehensive insights into failure mechanisms.

The fracturing and displacement of rocks during seismic activity generate weak EPs, whose abnormal precursory features are observed prior to earthquakes (Vallianatos and Tzanis, 1998; Vallianatos et al., 2004). The EP method is subsequently used in the study of rock instability evolution and is considered an effective tool for monitoring the fracturing behaviors of rocks (Triantis et al., 2006; Aydin et al., 2009). Many studies have suggested that the generation mechanisms of EPs include the piezoelectric effect (Yoshida and Ogawa, 2004), electrokinetic effect (Eccles et al., 2005), moving charged dislocations (MCD) (Vallianatos et al., 2004), crack tip charging effect (Li et al., 2021), and positive hole outflow effect (Freund et al., 2009), providing a reasonable explanation for the distribution of EPs at the microscopic scale. The MCD model, which explains EP generation, is highly insightful (Triantis et al., 2006). These findings suggest that native pore and microcrack defects in rocks facilitate the nucleation, development, and extension of microcracks under external loading. Moreover, the breaking of ionic bonds within the solid structure at crack surfaces leads to the formation of polarized crack edges, creating electric dipoles. The uneven distribution of these electric dipoles across the rock surface generates macroscopic EPs (Varotsos et al., 2002). Research has shown that external stresses applied to rocks induce variations in EPs, particularly as rocks approach the threshold of instability and failure (Shan et al., 2024b). In addition, EPs have been used to monitor groundwater flow laws and distribution, offering valuable insights into underground rock engineering and construction projects (Bai et al., 2021). Therefore, the EP method holds great promise as a tool for monitoring combined

coal-rock fractures and identifying coal-rock interfaces, providing valuable reference information for engineering applications.

However, most existing studies have focused on the EP response characteristics of single coal or rock bodies during failure, with limited research on the EP response in coal-rock combined samples during the failure process. Furthermore, accurate identification of coal-rock interface states remains a challenge, particularly in real-time monitoring under stress conditions, where the interface is in a localized damage or fracture state. Current methods face limitations in terms of cost and precision, hindering the safe and efficient operation of mining engineering projects. EP monitoring promises to provide more comprehensive information to improve the accuracy of coal-rock interface identification. Moreover, research on coal-rock interface recognition based on the EP method has not yet been conducted, and the distinguishing characteristics remain unclear. The catastrophic failure prediction of rock fracture is a critical aspect of coal-rock dynamic disaster prevention, and the multifractal features of EPs are expected to predict the combined coal-rock failure, while related studies remain scarce.

In this study, EP monitoring tests on coal-rock combined samples with two types of rock strengths during compression failure were conducted, including fine sandstone-coal and coarse sandstone-coal composites. The spatiotemporal response features of EPs during the progressive failure process of coal-rock combined samples were investigated. Two-dimensional (2D) EP contour maps and 3D spatial EP models were used to analyze the progressive failure process and accurate identification of the coal-rock interface. The force chain field and energy dissipation evolution were obtained from numerical simulations, and the relationship between them and the EP response was explored. Furthermore, multifractal characteristics based on EPs were utilized to identify the precursory information of combined coal-rock failure. In this study, EP technology was innovatively applied to the monitoring and early warning of coal-rock composite systems, providing valuable insights into the prevention and control of coal-rock dynamic disasters and offering new ideas and approaches for coal-rock interface identification.

2. Experimental scheme

2.1. Test system

As depicted in Fig. 1, the experimental test system includes an EP recording system, an AE recording system, and a uniaxial loading system. An MTS microcomputer-controlled 600 kN electrohydraulic servo testing machine, which supports both load-controlled and displacement-controlled loading modes, was used. The pressure is automatically adjusted to ensure full contact between the sample and the platens on both sides, effectively reducing the impact of sample surface nonuniformity on the test. A high-sensitivity wireless EP recorder with 32 channels, a wireless router, electrodes, and a microcomputer were used to capture EPs. The samples were manufactured by Jiangsu YiGe Biological Co., Ltd. This system enables recording and storing of the EPs captured in real time and with high accuracy. A 24-channel PCI-2 AE monitoring instrument from Physical Acoustics Corporation was used for the AE analysis. With the accompanying software, the system could record continuous AE waveform information, perform spectral analysis, and achieve 3D AE event spatial localization.

2.2. Sample preparation

The coarse sandstone, fine sandstone and coal used in this test were collected from the roof strata and coal seam of coal mines in Ordos, Inner Mongolia Autonomous Region, China. A large rock block was extracted from the mine and transported to the laboratory in core boxes. This block was then processed into standard cylindrical samples (ϕ50 mm $\times$ 50 mm) using hydraulic cutting and grinding machines, followed by drying in a constant-temperature drying oven. The end faces of the rock and coal samples were bonded together using XinWe6529 conductive adhesive (Shan et al., 2024a), forming combined samples with dimensions of ϕ50 mm $\times$ 100 mm. The adhesive with strong viscosity and excellent electrical conductivity ensures both firm bonding and effective electrical connection between different rock materials. The mechanical properties and resistivity of the thin adhesive layer at the coal-rock interface were negligible. This layer could serve as a scaled-down model of the actual coal-rock interface, and reflect the physical and mechanical properties of coal-rock composites in real coal mine engineering. Two types of combined samples were prepared, including fine sandstone-coal combined form denoted as RC-A, and coarse sandstone-coal combined form denoted as RC-H. Three parallel tests were conducted for the two sample groups, ensuring consistency in the size of the sandstone fractures and the cutting process, which minimized the randomness of the experimental results. The uniformity of the combined samples was evaluated by measuring the ultrasonic velocities using an ultrasonic velocity tester. Before each test, the equipment in the experimental system was calibrated to ensure consistency in instrument parameters and operating conditions. Efforts were made to maintain consistent environmental temperature and humidity for each test to minimize potential

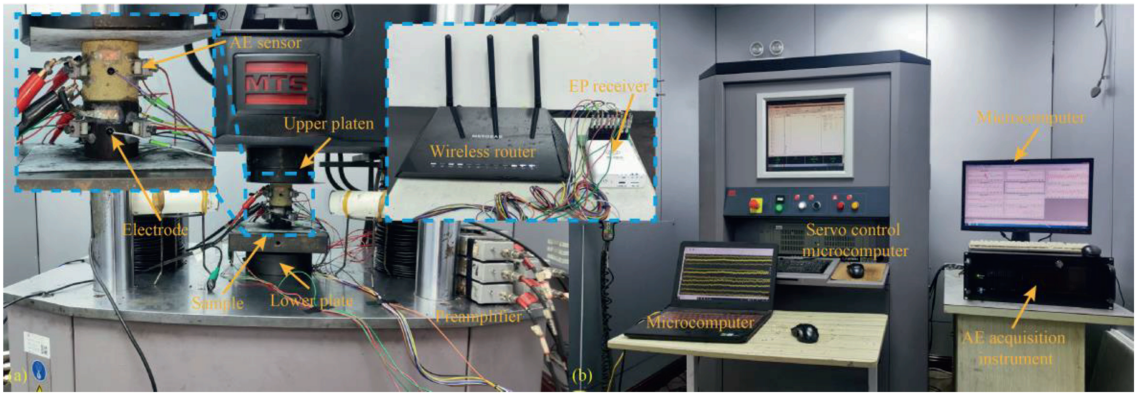

Fig. 1. Experimental test system for uniaxial compression test: (a) Uniaxial loading system, and (b) EP and AE recording systems.

Table 1
Physical and mechanical parameters of coal-rock combined samples.

Number	Rock type	Density (g/cm^3)	Wave velocity (km/s)	Peak stress (MPa)		Elastic modulus (GPa)	
				Value	Average	Value	Average
RC-A-1	Fine sandstone-coal	5.452	2.427	29.34	29.05	3.2	3.24
RC-A-2		5.421	2.404	27.52		3.14	
RC-A-3		5.435	2.427	30.28		3.37	
RC-H-1	Coarse sandstone-coal	5.096	2.226	19.91	20.75	2.47	2.5
RC-H-2		5.109	2.226	21.59		2.53	
RC-H-3		5.086	2.218	20.76		2.49	

environmental interference. The basic parameters of samples are listed in Table 1. The X-ray diffraction (XRD) analysis results for the residual samples are shown in Fig. 2. These results indicate that the fine sandstone consisted of quartz (44.7 %), microcline (14.7 %) and kaolinite (35.2 %), with small amounts of calcite (1.7 %) and biotite (3.7 %). The coarse sandstone primarily consisted of albite (36.7 %), quartz (23.5 %), and illite (11.8 %), with smaller amounts of kaolinite (8.1 %), vermiculite (0.8 %), and clinochlore (11 %). Moreover, the coal was primarily composed of a carbon matrix, with minor amounts of kaolinite (15.1 %), quartz (25.9 %), and calcite (59 %).

2.3. Test scheme

The displacement control method was used to move the loading plate, with a displacement rate of 0.2 mm/min. The sample was placed in the middle of the press plate, with a Neflon sheet inserted between the sample and the fixtures to reduce electrical noise. The sample end surfaces were in full contact and securely fixed between the fixtures. During the experiment, EPs, AEs, and stresses were continuously recorded. The placement of all the AE probes and copper electrodes is shown in Fig. 3. Eight NANO-30 AE sensors were glued to different locations on the sample surface using a specialized coupling agent. The AE sensors were labeled sequentially as AP-1 to AP-8. The peak definition time, hit definition time, and hit lockout time were fixed at 300 μs, 600 μs, and 900 μs, respectively. By using the pencil lead break method to detect the AE localization accuracy, the AE localization error, which indicated the error distance between the test point and location point, was less than 2 mm, thereby achieving the desired AE localization results. When loading, the preamplifier and threshold values were set to 40 dB, and the sampling rate was set to 1 MSPS. For EP measurements, 10 electrodes were used as test electrodes, a common electrode, and a reference electrode, all of which were copper electrodes. The test electrodes, labeled Ch-1 to Ch-10, were arranged at different locations on the rock surface and attached using medical conductive adhesive. The sampling frequency of EPs was set to 500 Hz, with a common frequency filter of 50 Hz and a low-pass filter of 30 Hz. The EP recorder has a resolution of up to 0.0224 μV and a common-mode rejection ratio greater than or equal to 120 dB, effectively mitigating power noise and ground interference. The current impedance of the EP recorder exceeds 1 GΩ, allowing for more accurate capture of subtle signal variations. The electrodes detected weak EPs on rock surfaces. EPs were transmitted through the signal receiver and wireless router to a computer for further analysis.

3. Results

3.1. EP response laws

To facilitate a clear analysis of the temporal evolution of EPs, the background EP value is subtracted from the measured EPs under stress, while preserving their original polarity. Fig. 4 depicts the temporal response characteristics of EPs and AEs for sample RC-A-1 and sample RC-H-1 during failure. The EP response characteristics of the two samples are similar at different loading stages. Moreover, the four different deformation stages are defined on the basis of the variations in the slopes of the stress-strain curves. During the compaction stage (Stage I), the stress-strain curve is concave, the AEs are relatively weak, and the primary damage mechanism is the closure of pre-existing pores and microcracks within the samples. The EPs remain stable, showing a slow upward trend while maintaining a low intensity level. Moreover, the AE hit rates of both coal and rock are nearly negligible, indicating minimal microfracturing within the combined

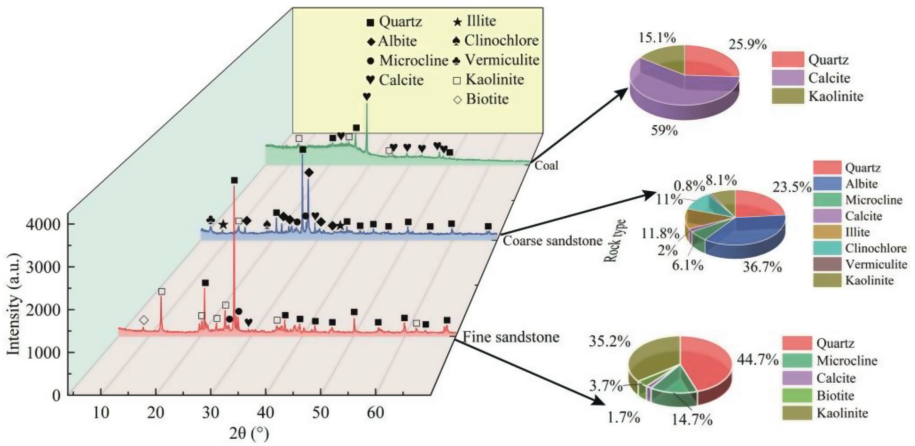

Fig. 2. Mineral composition and content of combined coal-rock samples obtained by XRD test.

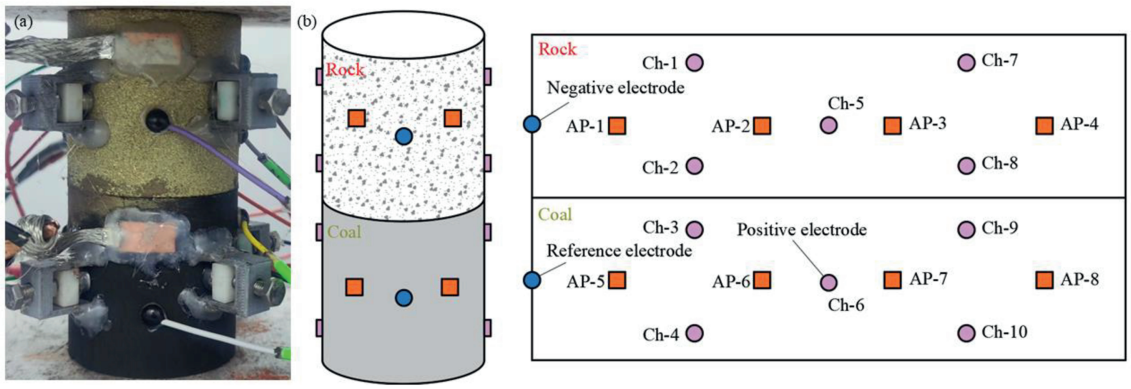

Fig. 3. Sensor location on the sample surface: (a) Physical image of sample and sensors, and (b) Detailed layout positions of AE sensors and electrodes.

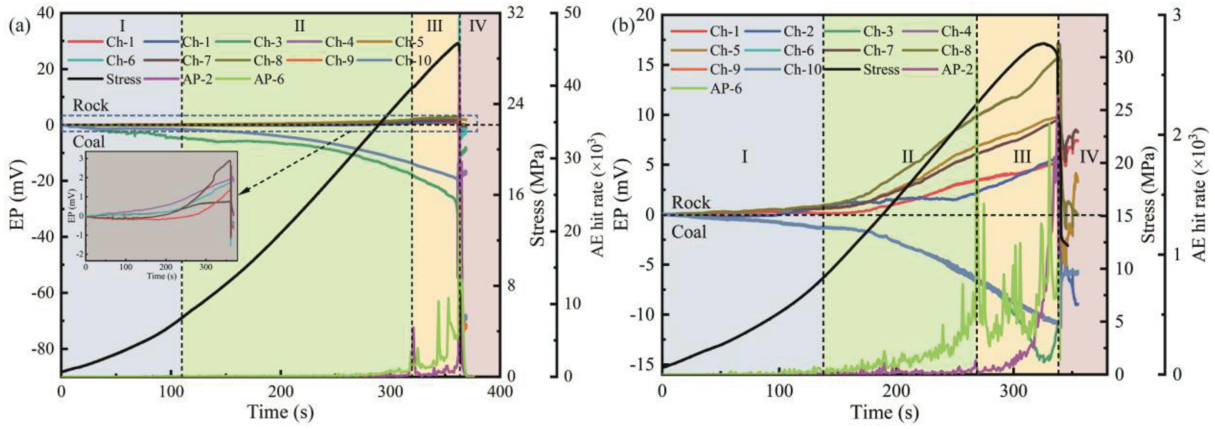

Fig. 4. Evolution characteristics of EPs and AEs of combined samples during failure: (a) Sample RC-A-1, and (b) Sample RC-H-1.

samples. In the elastic stage (Stage II), stress varies linearly with the strain, the AEs gradually increase, and fractures are distributed uniformly throughout the samples. The EPs exhibit a linear growth trend, and their intensities significantly increase and show minimal fluctuations. During this stage, the AE hit rates of the coal and rock begin to increase slowly, reflecting the random and uniform initiation of microcracks within the samples. After the plastic stage (Stage III), the stress-strain curve demonstrates nonlinear behaviors, and both the density and intensity of the AEs increase dramatically. The microcracks in the samples continue to grow, coalesce, and become macroscopic cracks. The EPs increase rapidly and are accompanied by large fluctuations. At this moment, the coal-rock combined samples experience slight stress drops, whereas the AE hit rates exhibit an accelerating upward trend accompanied by local fluctuation peaks. This finding indicates the dense appearance, connection, and coalescence of microcracks, with localized relaxation phenomena being caused by dislocation and slip within microcrack clusters. Notably, the AE intensity and fluctuation amplitude of the coal are significantly greater than those of the rock, suggesting that the coal experiences more severe damage and greater internal degradation. In the post-peak failure stage (Stage IV), the samples undergo main fracture, the AE hit rate reaches its peak, and macroscopic cracks become evident. The EPs show a sharp instantaneous change, caused by the large-scale instantaneous discharge along newly formed crack surfaces. At this stage, the microcrack clusters within the samples interconnect to form macroscopic cracks, leading to structural failure.

As shown in Fig. 4, for both combined samples, the EPs from the rock and coal exhibit opposite directions, which are reflected in the opposite polarity and trend of the EP values. Since all the test electrodes use the same common electrode, this phenomenon indicates that the potential difference generated between the rock and coal is opposite. For sample RC-A-1, the EP intensity of the coal is significantly greater than that of the rock. In contrast, for sample RC-H-1, the EP intensities of the coal and rock are comparable. It can be attributed to the strengths of fine sandstone being much greater than that of coal. For sample RC-A-1, only the coal experiences severe damage, whereas the fine sandstone exhibits linear elastic rebound when it fails, resulting in a greater accumulation of charges in the coal and a greater potential difference between measurement points. For sample RC-H-1, both the coarse sandstone and coal undergo significant damage, with crack-induced charge accumulation occurring in both components. Consequently, the potential difference between the components is relatively small. The EP responses of the two kinds of coal-rock combined samples significantly differ. The EP variation in coarse sandstone is more pronounced, whereas the EP variation in fine sandstone is relatively small. Moreover, compared with fine sandstone, coarse sandstone has a faster change rate, suggesting that the differences in their EP responses may be due to two factors. On one hand, more severe fractures occur in coarse sandstone, where the expansion of the crack network generates a large amount of charges. On the other hand, the larger particle size of coarse sandstone results in stronger friction between particles, making it more prone to noticeable charge migration and EP changes under stress.

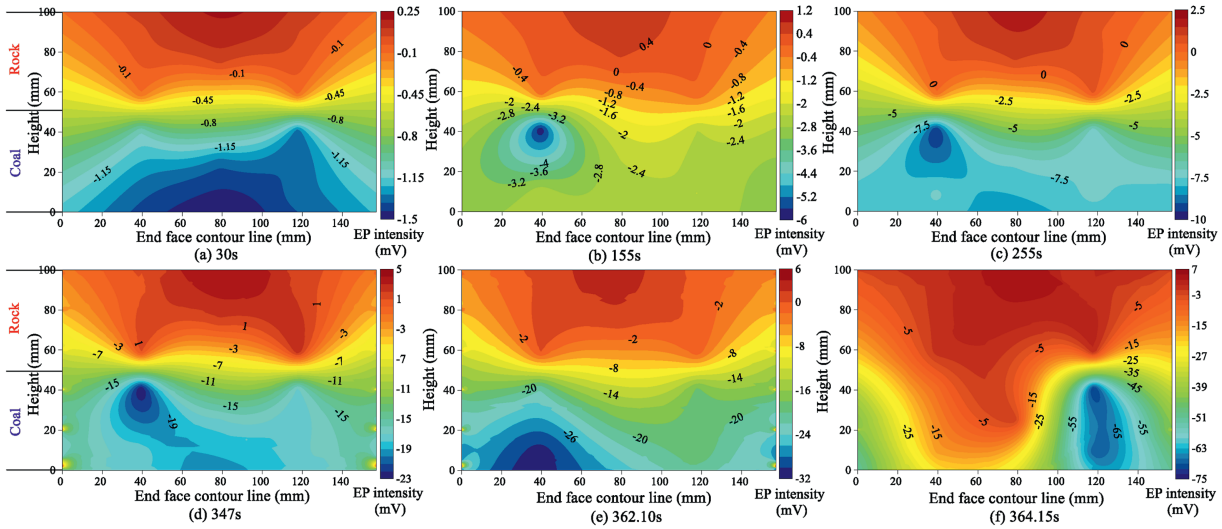

Fig. 5. Evolution of EP cloud maps of sample RC-A-1 at various loading moments.

3.2. Evolution of the surface EP cloud map

To further analyze the EP distribution of the whole combined sample, the lateral surface of each sample is unfolded along the line connecting the common electrode and the reference electrode. Based on the evolution of EPs at all testing electrodes, EP cloud maps of samples RC-A-1 and RC-H-1 at six representative moments during the experiment are shown in Figs. 5 and 6. The EP values corresponding to the rock region at heights of 50–100 mm are almost exclusively greater than zero, whereas the values in the coal region at heights of 0–50 mm are predominantly less than zero. In addition, as the height increases, the absolute EP values first decrease but then gradually increase, indicating unidirectional variation in the difference in EP along the vertical axis of the coal-rock combined sample. Since the EP level of rock is higher than that of coal, according to the Ohm's law and charge conservation law (Purcell and Morin, 2013), the weak current flow direction in the combined coal-rock is from the rock, across the interface, and into the coal. This observation aligns with the findings of Shan et al. (2024a).

For the EP cloud maps at different loading stages, prior to failure, the EP intensity near the coal-rock interface is close to zero and remains low, forming a green low-intensity signal band. Above the coal-rock interface, the EPs increase progressively with increasing height, whereas below the coal-rock interface, the EPs decrease with decreasing height. Therefore, the distribution of EPs can be used to accurately identify the location of the coal-rock interface, which is highly important for mining engineering design and disaster prevention. When the main failure occurs, the EPs of the combined samples continue to increase with increasing height. However, the EP level distribution becomes noticeably imbalanced. Specifically, the green low-intensity signal band undergoes significant changes and no longer remains parallel to the interface, instead bending into the coal or rock regions. In particular, for sample RC-A-8, the rock area remains in the high-intensity signal zone, while the left part of the coal area has a high-intensity signal zone, and the right part of the coal area has a low-intensity signal zone. It indicates that crack propagation in rock is limited and remains stable, whereas that in the coal is severely damaged. For sample RC-H-15, the green low-intensity signal band is no

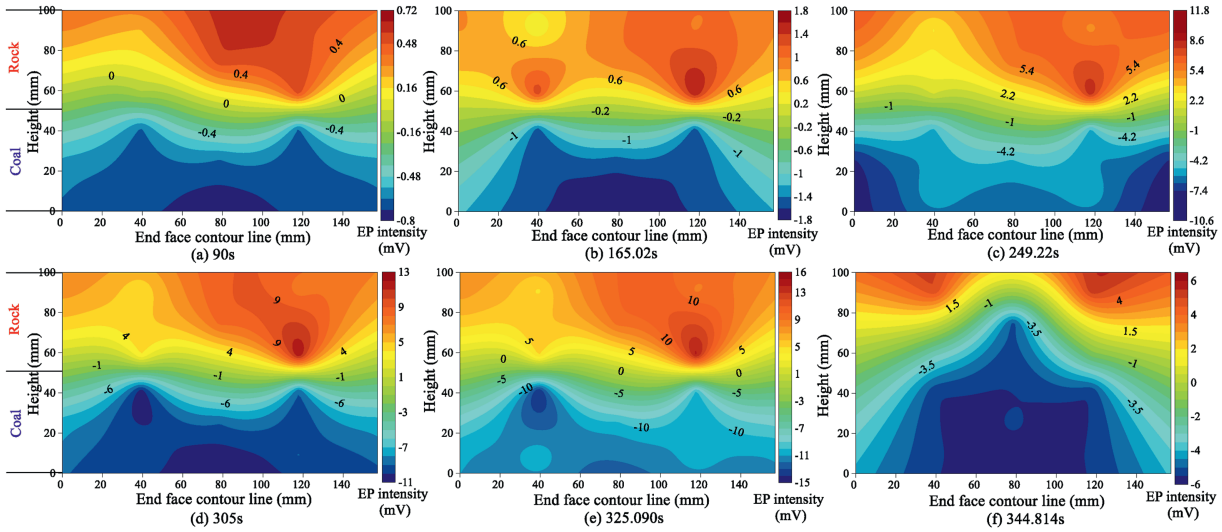

Fig. 6. Evolution of EP cloud maps of sample RC-H-1 at various loading moments.

longer parallel to the coal-rock interface, but partially bends upward into the rock. The rock exhibits large areas of both low-intensity and high-intensity signal bands, while the coal is almost entirely characterized by low-intensity signal band. It indicates that both the rock and coal bodies undergo significant damage, which is consistent with the fracture characteristics of the sample. Therefore, the EP field of combined coal-rock sample significantly changes during instability and failure. The above analysis reveals that the EP cloud map can clearly characterize the fracture features of coal-rock combined samples.

3.3. Fracture features and 3D EP model

Fig. 7a and c illustrates the evolution of AE event distributions of samples RC-A-8 and RC-H-15, along with the failure images of the samples. Meanwhile, the spheres represent AE events, with their size and color indicating the energy level of the AE events. The evolution of the AE events clearly reflects the damage states of samples during the progressive failure process. The failure processes of samples RC-A-8 and RC-H-15 significantly differ because of the varying strength of the rock, which results in distinct overall failure processes. For sample RC-A-8, the strength of the fine sandstone is greater than that of the coal. Consequently, more high-energy AEs are concentrated in the coal, indicating that the coal experiences severe internal damage. Due to the lower homogeneity of the coal, localized failures first occur, and then expand to affect the entire coal component. Moreover, the fine sandstone remains relatively intact during the loading process until failure occurs, when it exhibits a linear rebound phenomenon. For sample RC-H-15, the strength of the coarse sandstone is slightly greater than that of the coal, resulting in significant damage to both the coarse sandstone and coal. Localized damage initially occurs in the lower part of the coarse sandstone and in the middle-lower part of coal. In particular, many microcracks are generated in the middle-lower coal and extend upward and eventually penetrate the coal-rock interface into coarse sandstone, leading to damage and failure of coarse sandstone.

The AE waveforms recorded for the coal-rock combined samples are subjected to fast Fourier transform (FFT) to obtain their main frequencies and amplitudes. Fig. 7b and d illustrates the changes in the dominant frequencies and amplitudes of AEs in the coal and rock regions. Generally, AEs with high main frequencies indicate small-scale fractures within the rock, while AEs with lower main frequencies suggest larger-scale fractures (Wang et al., 2024). In the early loading stage, many AE activities with high frequencies and low amplitudes are observed, indicating the occurrence of small-scale microfractures within the samples. With increasing stress, the AE amplitude gradually increases, and the

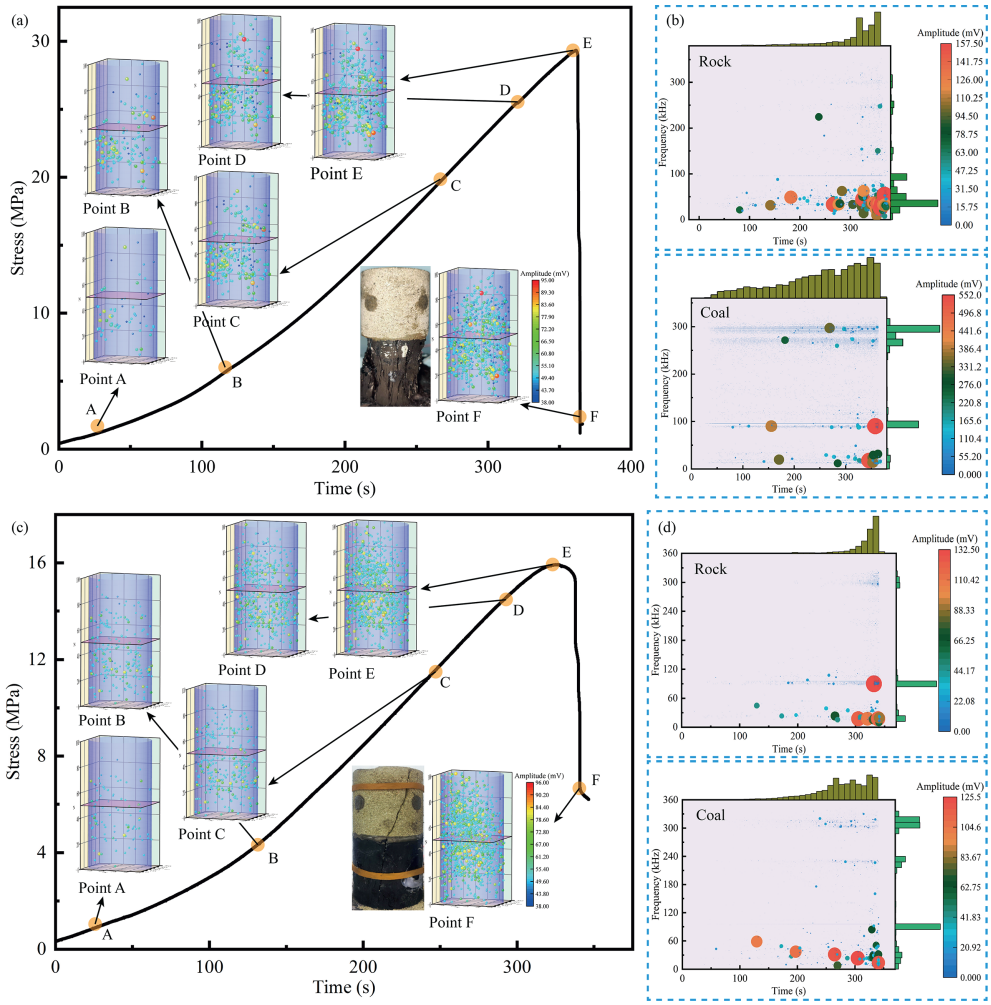

Fig. 7. Evolution characteristics of AE event distribution and frequency spectrum: (a) AE event distribution of sample RC-A-1, (b) Frequency spectrum characteristics of sample RC-A-1, (c) AE event distribution of sample RC-H-1, and (d) Frequency spectrum characteristics of sample RC-H-1.

AEs predominantly appear in the low-frequency and mid-frequency bands. It indicates that, in addition to the formation of numerous small-scale fractures, larger-scale fractures also begin to develop within the sample. During the plastic stage, AEs are primarily concentrated in the mid-frequency and low-frequency bands with significantly increased amplitudes, especially as the main failure approaches. It suggests the occurrence of numerous large-scale fractures within the sample. Concurrently, high-frequency AEs persist throughout the process, reflecting the continuous activities of small-scale fractures. Fig. 8 presents the AF/RA distribution characteristics of the AEs during the failure process, along with the tensile-shear failure discrimination results. The ratio of the average frequency (AF) to the rise time/amplitude ratio (RA) is used as an indicator to differentiate between tensile failure and shear failure modes. Based on previous references (Shan et al., 2024b), after testing different values of k as the threshold values, we find that $k = 2$ best corresponds to the failure and fracture characteristics of the coal-rock composite samples under uniaxial compression in this study. Specifically, when AF/RA$\geq$2, tensile failure occurs, whereas when AF/RA<2, shear failure occurs. For the two types of combined coal-rock samples, significant tensile failure occurs in both coal and rock. Meanwhile, compared with coal, rock has a greater proportion of shear failure. It is because the rock experiences tensile splitting failure that is initiated near the interface, while the coal undergoes overall shear failure.

To provide a clear analysis of the relationship between the spatial response characteristics of EPs and failure evolution of coal-rock combination sample when failure occurs, 3D EP model images are constructed through an interpolation method using the electrode network formed by all testing channels. Fig. 9 shows the 3D EP model images at specific moments. The colors in the figures represent EP levels, and the color scale is standardized across the same EP range to facilitate temporal comparisons. For sample RC-A-1, during the early loading stages (Points *A*, *B*, and *C*), the EPs exhibit a relatively uniform distribution, with the entire sample predominantly appearing in red. Meanwhile, the EPs in the coal and near the coal-rock interface gradually transition from deep red to light red, indicating a continuous decrease in the EP intensity within the coal. In the plastic stage (Points *D* and *E*), the EP distribution of the combined samples significantly changes, with the EP model in the coal shifting from orange at the onset of the plastic stage to yellow near the main failure portion. It is attributed to the formation of numerous microcracks in the plastic stage, generating substantial charges because of the MCD and crack tip charging effect. At the moment of main failure (Point *F*), the overall EP distribution changes significantly, with large blue-green areas observed in the coal and small yellow-orange areas in the rock. It indicates severe damage to the coal, while the fine sandstone experiences only minor damage near the interface, which is consistent with the failure characteristics of sample RC-A-1 shown in Fig. 8. For sample RC-H-1, during the compaction stage (Points *A* and *B*), the overall EP distribution of the coal-rock combined samples appears cyan-green, with relatively low EP intensity. After entering the elastic stage (Point *C*), the EP distributions of the coarse sandstone and coal noticeably differ. Large blue areas appear in the coal region, a green band is observed at the coal-rock interface, and extensive orange areas are present in the rock region. In the plastic stage (Points *D* and *E*), the EP distribution of the coarse sandstone changes significantly, transitioning from orange to red, while the EPs of the coal remain predominantly blue. At the failure moment (Point *F*), the EP distribution undergoes an overall transformation, and blue areas are widely distributed across both the coarse sandstone and coal. The coarse sandstone shows

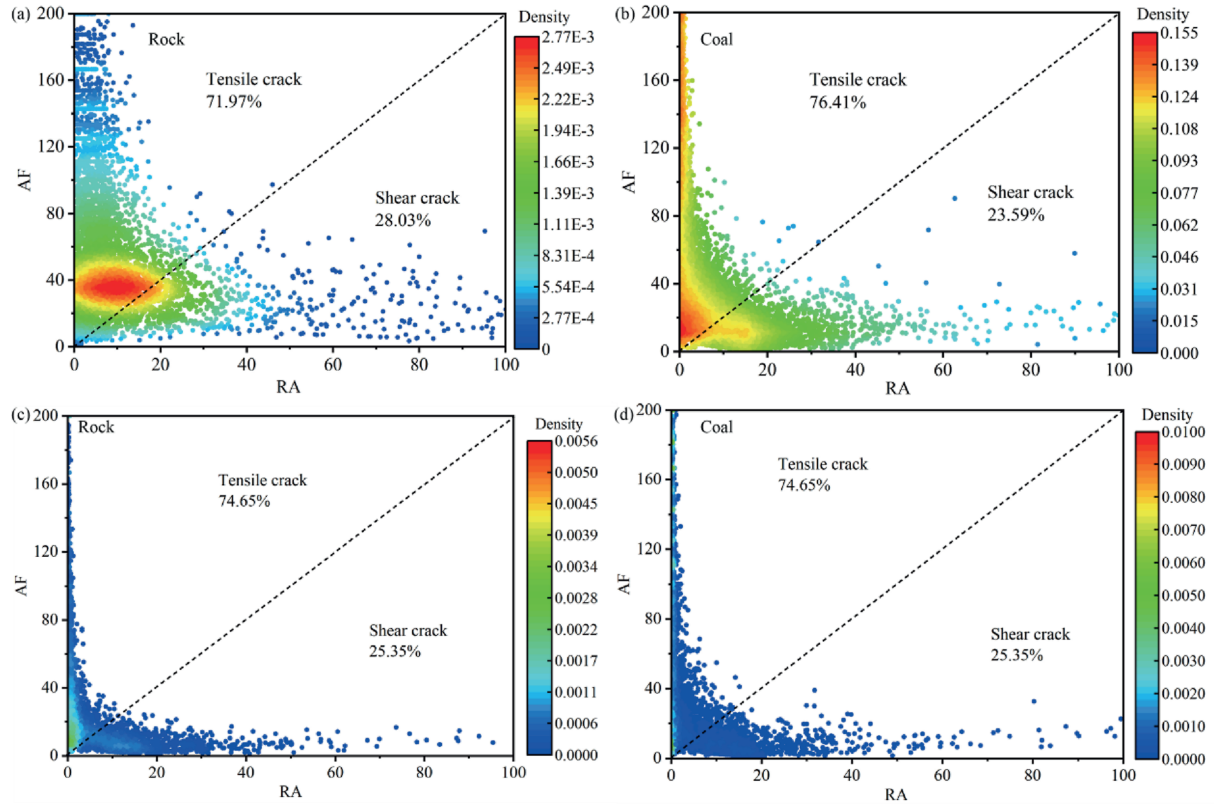

Fig. 8. Fracture modes of combined samples in the whole failure process: (a) Rock of RC-A-1, (b) Coal of RC-A-1, (c) Rock of RC-H-1, and (d) Coal of RC-H-1.

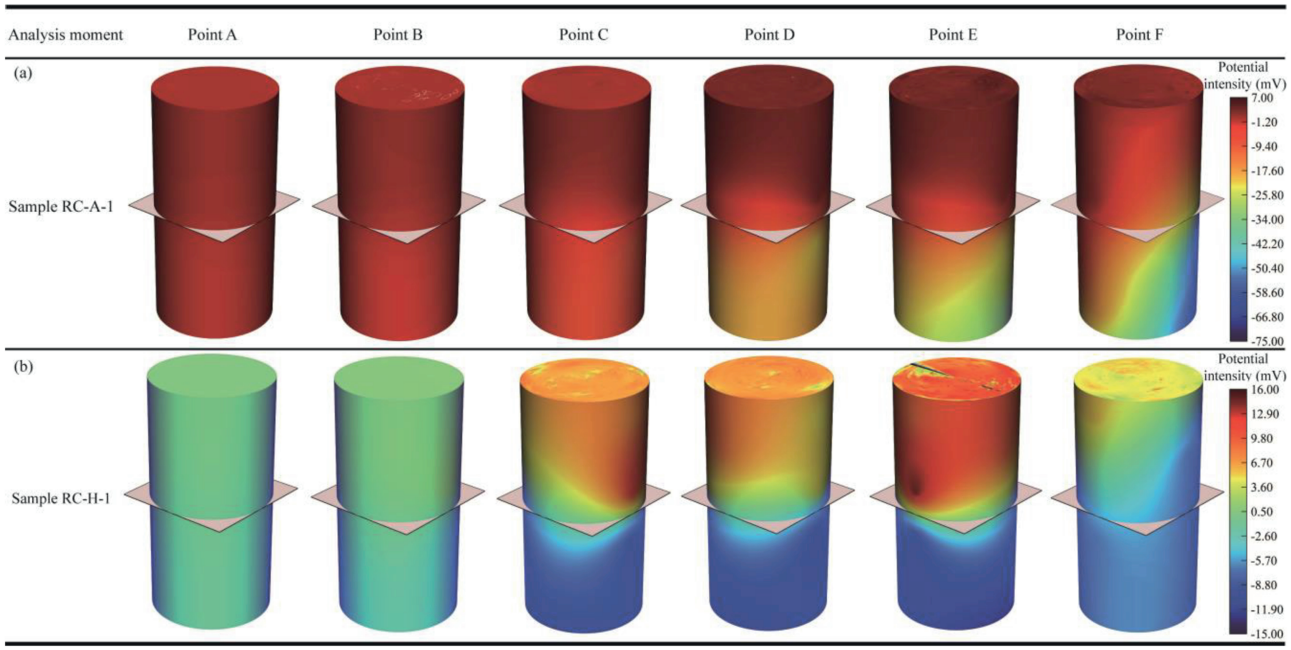

Fig. 9. Evolution characteristics of 3D EP model images under various typical uniaxial stresses: (a) Sample RC-A-1, and (b) Sample RC-H-1.

various colored strips, while subtle differences in the blue areas on the coal can be observed. It indicates that both the coarse sandstone and coal experience severe damage, which is consistent with the results shown in Fig. 8. In summary, the 3D EP model can effectively capture the progressive failure characteristics and facilitate location identification of coal-rock interface. Moreover, this model serves as a more intuitive method for analyzing the fracture states of combined samples.

4. Discussion

4.1. Relationship between numerical results and EP response

A numerical model was developed using PFC2D to analyze the force chain evolution and damage laws of the two types of combined coal-rock samples during loading and deformation. This model provides insights into the macroscopic fracture behaviors of rock particle deformation, degradation, and failure from a microscopic perspective. Based on numerical simulations and experimental results, the response mechanisms of the EPs of coal-rock combined samples when failure occurred are further analyzed. With the help of the macroscopic mechanical parameters obtained from laboratory experiments, a standard combined coal-rock sample model with a diameter of 50 mm and a height of 100 mm is established, as shown in Fig. 10a. The coal-rock height ratio is set to 1. The minimum particle radius is 0.2 mm, and the particle size ratio is 1.5 with uniformly distributed particle sizes. Fig. 10 illustrates the model configuration and the contact bond network. The coal and rock domains adopt the parallel bond model for their internal structures (Fig. 10b), while the coal-rock interface is modeled using the linear contact model (Fig. 10c). External force boundary constraints are applied to both end faces of the model, with the two ends being compressed at a constant rate of 0.2 mm/min to simulate the axial deformation of the sample. Through continuous adjustment of the mechanical parameters and stress-strain curves, the microscopic parameters for each model are determined, as shown in Table 2. E_c and $\overline{E}$ represent the contact modulus and parallel bond modulus, K_n/K_s and $\overline{K}_n/\overline{K}_s$ represent contact stiffness ratio and parallel bond stiffness ratio, $\overline{\sigma}_c$, $\overline{\tau}_c$ and μ represent normal bond strength, tangential bond strength and friction factor. The damage pattern, force chain field and contact force field for types RC-A and RC-H are shown in Fig. 11. Based on the MCD model, crack tips generate and accumulate many electric dipoles, altering the distribution of dipoles on the rock surface and thereby forming macroscopic EPs. In regions where the sample undergoes localized fracture, particularly near the crack tips, a strong force chain field forms with a relatively sparse force chain distribution. It suggests that this area is in an unstable state, and many electric dipoles accumulate. Therefore, the distribution features of force chain field are significantly related to the EP response.

There is an obvious difference in crack propagation and force chain distribution between types RC-A and RC-H, which is related to rock strength. For sample type RC-A, fractures primarily occur within the coal, where cracks initiate and cause collapse on both sides, while only minimal rock fragments detach from the sandstone near the interface on the right side. Sparse force chain regions are distributed in areas with dense crack propagation, and are primarily concentrated within the coal. As a result, a greater accumulation of electric dipoles occurs within the coal, leading to a higher EP level during fracture. It is consistent with the features of 3D EP model shown in Fig. 9a. For the sample type RC-H, noticeable cracking occurs within both the coal and coarse sandstone, along with the detachment of small rock blocks. The main crack propagates through the coal-rock interface, and sparse force chain fields appear in both coal and coarse sandstone. It indicates that many electric dipoles form in both materials, leading to changes in the EP distribution, as evidenced by the marked increase in EP levels of both materials shown in Fig. 9b. Therefore, the EP response features are clearly related to the force chain distribution.

The deformation of coal-rock combined samples involves exchanges of matter and energy with the external system, particularly the release of dissipated energy and frictional energy, accompanied by various geophysical signal energies, such as

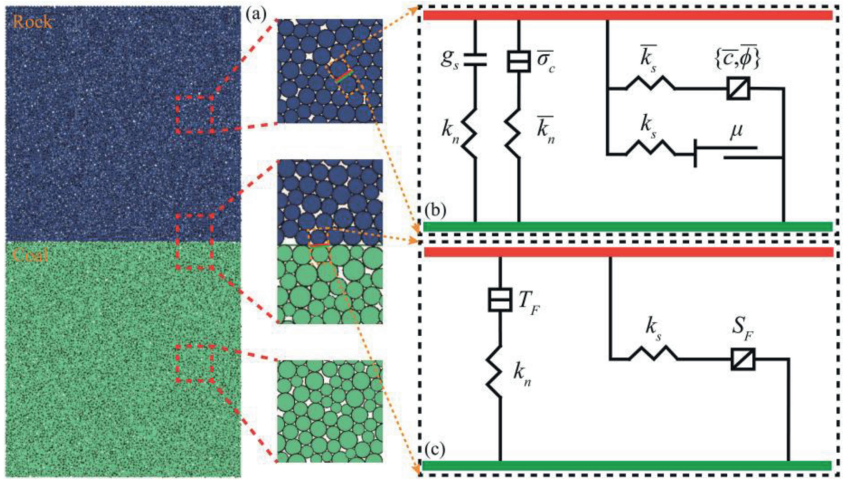

Fig. 10. Numerical model for the uniaxial compression test of combined coal-rock: (a) Numerical model arrangement, (b) Schematic diagram of parallel bond model, and (c) Schematic diagram of linear contact model.

Table 2
Mesoscopic parameters of the numerical model.

Group	Type	E_c (GPa)	K_n/K_s	$\overline{E}$ (GPa)	$\overline{K}_n/\overline{K}_s$	$\overline{\sigma}_c$ (MPa)	$\overline{\tau}_c$ (MPa)	μ
RC-A	Rock	7.2	2.2	7.2	2.2	32	48	0.5
	Coal	1.3	2.4	1.3	2.4	12	18	0.5
RC-H	Rock	3.5	2.1	3.5	2.1	14	21	0.5
	Coal	1.3	2.4	1.3	2.4	12	18	0.5

electromagnetic energy and acoustic energy. In the PFC2D simulations, energy is categorized into model component energy and contact energy. The model component energy includes the total boundary energy on the walls, the kinetic energy, and the damping energy of particles, while the contact energy encompasses strain energy, damping energy, and sliding friction energy between different types of contacts. The PFC simulation fully considers the effects of cracks, where the stored strain energy is completely released upon contact fracture and separation, which is consistent with actual fracture behaviors. Fig. 12 illustrates the evolution curves of energy dissipation in the two models. During the initial loading stage, almost all of the total energy is converted into strain energy, with only a small proportion being attributed to frictional energy, dissipated energy, and kinetic energy. Upon entering the plastic stage, the contributions of frictional energy and dissipated energy gradually increase, while kinetic energy remains nearly zero. After reaching the peak stress, the frictional energy, dissipated energy, and kinetic energy tend to accelerate, while strain energy decreases. To further analyze the relationship between EPs and energy dissipation, the experimentally obtained cumulative EP value and cumulative AE hit value in Fig. 13 are compared with the energy dissipation curves in Fig. 12. In this study, their changes are consistent with the energy dissipation behaviors of the combined samples. Therefore, the cumulative EP value and cumulative AE hit value serve as indicators of internal damage evolution within the rock. During the early loading period, cumulative EP value and cumulative AE hit value are small, while during the later loading period, they exhibit accelerated growth, corresponding to the release of dissipated energy within the samples.

4.2. Multifractal characteristics of EPs

The rock failure process exhibits typical nonlinear and self-similar characteristics. The use of multifractal spectra allows for the exploration of distribution patterns across different scales, providing a method for characterizing the heterogeneity and intrinsic complexity of physical signals (Higuchi, 1988; Cheng et al., 2020b). To further investigate the crack damage states and evolution processes within the two components of the combined samples, the multifractal characteristics of EPs in the coal and rock are investigated. The multifractal spectrum $f_m(\alpha)$-α_m reflects the heterogeneity of the signal distribution. A larger spectrum width $\Delta\alpha_m = \alpha_{max} - \alpha_{min}$ indicates greater fluctuations in the signal distribution and more pronounced multifractal characteristics (Wang et al., 2024). In addition, $\Delta f_m = f(\alpha_{max}) - f(\alpha_{min}))$ represents the frequency relationship of signals associated with different fracture scales. A smaller Δf_m implies a greater proportion of large-scale fracture signals, whereas a larger Δf_m corresponds to a greater proportion of small-scale fracture signals. Moreover, Δf_m can serve as a measure of the dominant mechanisms driving EPs. When $\Delta f_m>0$, weak micro-mechanisms dominate, whereas $\Delta f_m<0$ indicates strong micro-mechanisms are predominant.

In this section, the EPs of coal-rock combined samples are analyzed comprehensively using the multifractal singularity spectrum based on the box-counting dimension method. The time-series sequence of EPs, denoted as $\{x(i)\}$, is split into N subsets, each with a length of ξ. The partition function (statistical moment) can be expressed as follows (Qiu et al., 2020):

$$X_q(\xi) = \sum P_i(\xi)^q \propto \xi^{\tau(q)} \tag{1}$$

where ξ is a variable, and $\tau(q)$ represents the mass exponent. In addition, based on Eq. (1), $\tau(q)$ can be calculated as follows:

$$\tau(q) = \lim_{\xi \to 0} \frac{\ln X_q(\xi)}{\ln \xi} \tag{2}$$

Given that the sequence $\{x(i)\}$ exhibits multifractal characteristics, $\ln X_q(\xi)$ and $\ln\xi$ satisfy a linear relationship (Hu et al., 2014). The generalized fractal dimension D_q can thus be expressed as follows:

$$D_q = \frac{\tau(q)}{q-1} = \frac{\ln X_q(\xi)}{(q-1)\ln \xi} \tag{3}$$

The generalized fractal dimension D_q for different values of q represents various aspects of the fractal properties. By applying the Legendre transform to Eq. (3), the following can be obtained:

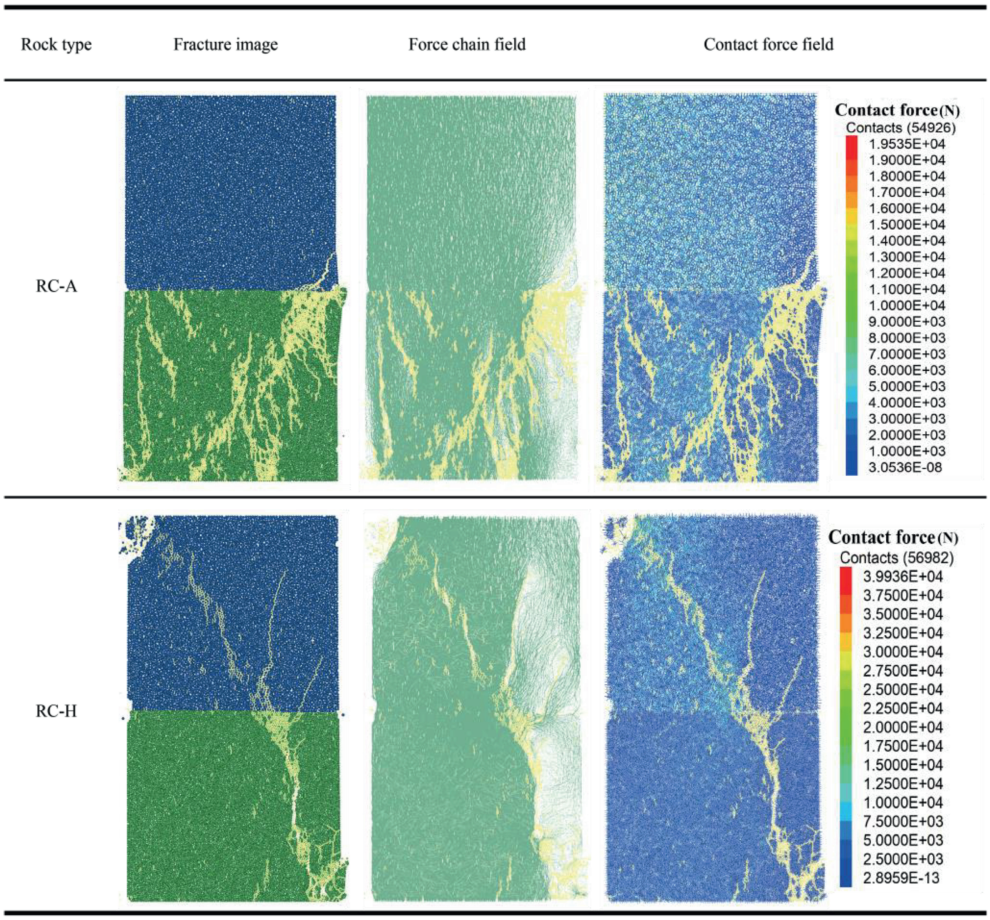

Fig. 11. Cracks, force chain fields and contact force fields of combined samples.

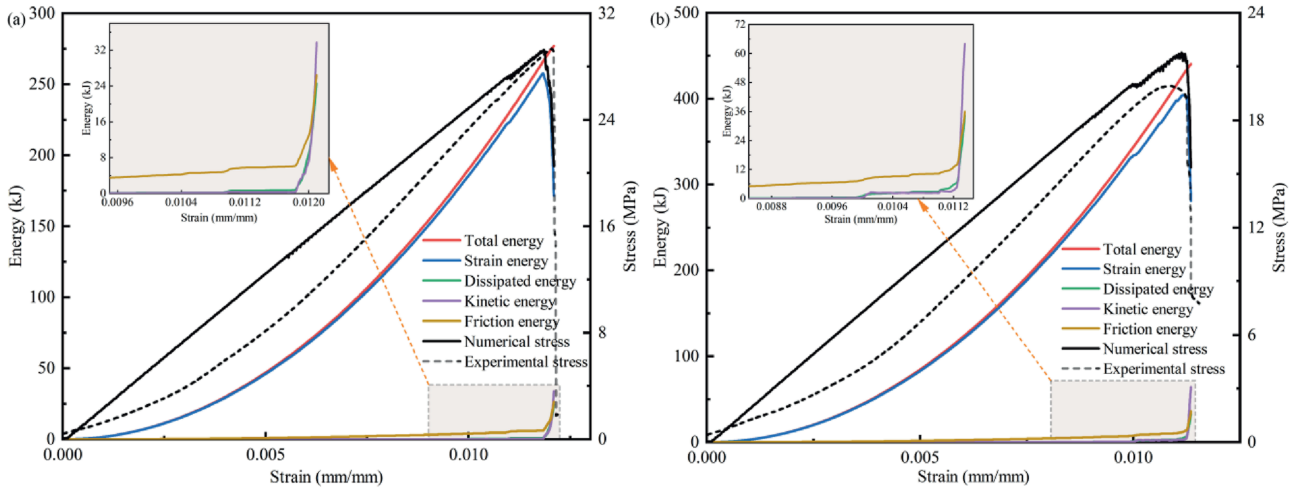

Fig. 12. Energy evolution characteristics of numerical models during the failure process: (a) Type RC-A, and (b) Type RC-H.

$$\alpha = \frac{\mathrm{d}(\tau(q))}{\mathrm{d}q} = \frac{\mathrm{d}}{\mathrm{d}q}\left(\lim_{\xi \to 0} \frac{\ln X_q(\xi)}{\ln \xi}\right) \tag{4}$$

The multifractal spectrum becomes stable once $|q|$ reaches a specific value. α represents the singularity, reflecting the uneven evolution of the subset probability distribution with changes in scale ξ. $f(\alpha)$ denotes the rate at which the number of subsets per unit increases as ξ decreases, representing the fractal dimension of ξ.

Fig. 14 presents the multifractal spectra of EPs at selected EP measurement points of coal-rock combined samples during failure. The EPs in both coal and rock exhibit multifractal characteristics, satisfying scale invariance. The multifractal curves display a right-hook shape with relatively large $\Delta\alpha$ values, indicating

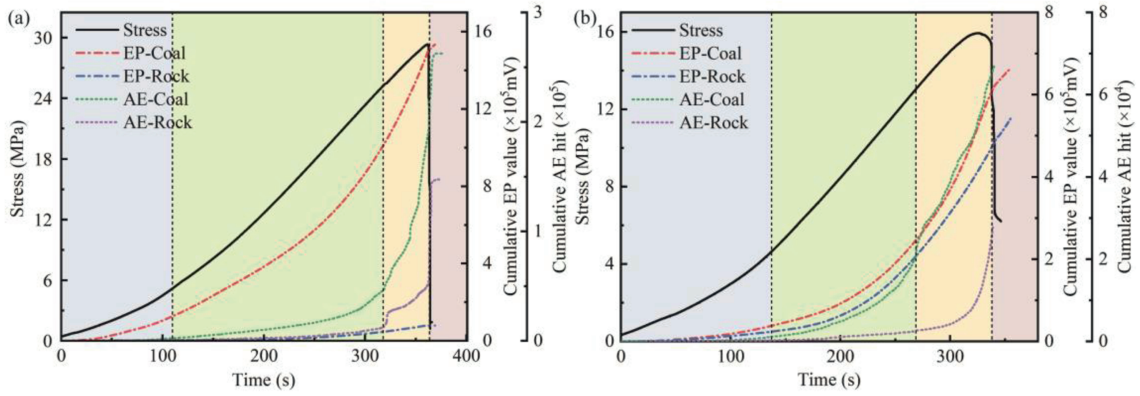

Fig. 13. Evolution characteristics of cumulative EP value and cumulative AE value: (a) Sample RC-A-1, and (b) Sample RC-H-1.

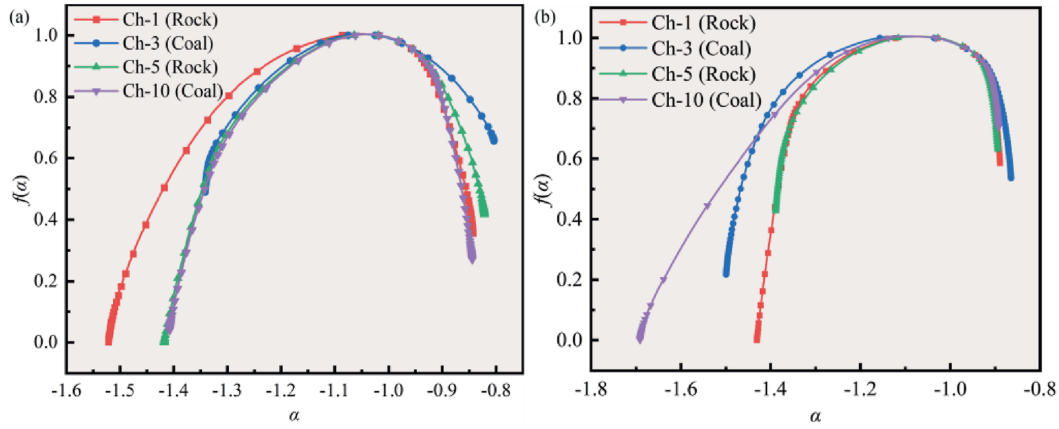

Fig. 14. Multifractal spectrum of failure evolution based on EP analysis: (a) Sample RC-A-8, and (b) Sample RC-H-15.

significant changes and nonlinear characteristics of the EPs during failure. For sample RC-A-1, the $\Delta\alpha$ value of the coal is greater than that of the rock, while the Δf value is smaller. It suggests that the EPs in the coal exhibit more pronounced changes and stronger nonlinear characteristics. This behavior arises from the significantly higher strength of the rock than that of the coal, leading to elastic rebound in the rock and severe failure in the coal. For sample RC-H-1, there are no significant difference in $\Delta\alpha$ and Δf values between the rock and coal. It is because the strengths of coal and rock are comparable, resulting in both severe and evident failure.

Fig. 15 illustrates the evolutions of $\Delta\alpha$ and Δf for channels Ch-1 and Ch-3 during the failure processes of the two samples. Their evolutions are strongly influenced by the stress states of the samples. During the compaction stage, the absolute values of $\Delta\alpha$ and Δf are relatively high and exhibit significant fluctuations, gradually decreasing over time. This behavior is attributed to the locally uneven stress distribution and the sudden application of stress, which causes the closure of existing micropores and cracks and triggers some fractures. This process generates a substantial amount of charges because of the crack tip charging effect and MCD, and it leads to instability in the EPs. In the elastic stage, both $\Delta\alpha$ and Δf stabilize at relatively low levels with minimal fluctuations. It indicates that relatively few fractures occur during this stage and that the fractures are uniformly and randomly distributed, producing only a small amount of charge primarily through the piezoelectric effect. In the plastic stage, $\Delta\alpha$ gradually increases, while Δf decreases progressively. This behavior is associated with the development of microcracks within the samples. Consequently, the crack tip charging effect and MCD generate a large amount of charges, leading to a significant increase in EPs. These results demonstrate that a larger $\Delta\alpha$ indicates greater variations in the EP sequence, highlighting more distinct differences. Conversely, a smaller Δf reflects stronger intensity differences and more pronounced nonlinear characteristics in the EP sequence. Before sample failure, both $\Delta\alpha$ and Δf significantly increase, which can be used to predict sample failure. For the same sample, the precursory points for $\Delta\alpha$ and Δf on the rock and coal components appear simultaneously. For sample RC-A-1, the precursory point appears at 358.77 s, providing an advanced prediction time of 4.53 s. For sample RC-H-1, the precursory point occurs at 331.83 s, with an advanced prediction time of 5.89 s. Therefore, $\Delta\alpha$ and Δf based on EPs can serve as effective precursory indicators for combined coal-rock.

4.3. Applications and prospects

Early identification of coal-rock interfaces helps optimize mining engineering designs and assess the hydrogeological structure within the mine, preventing coal-rock dynamic disasters, such as water inrush, gas explosions, and collapses caused by unclear coal-rock interfaces. This study applies EP monitoring to

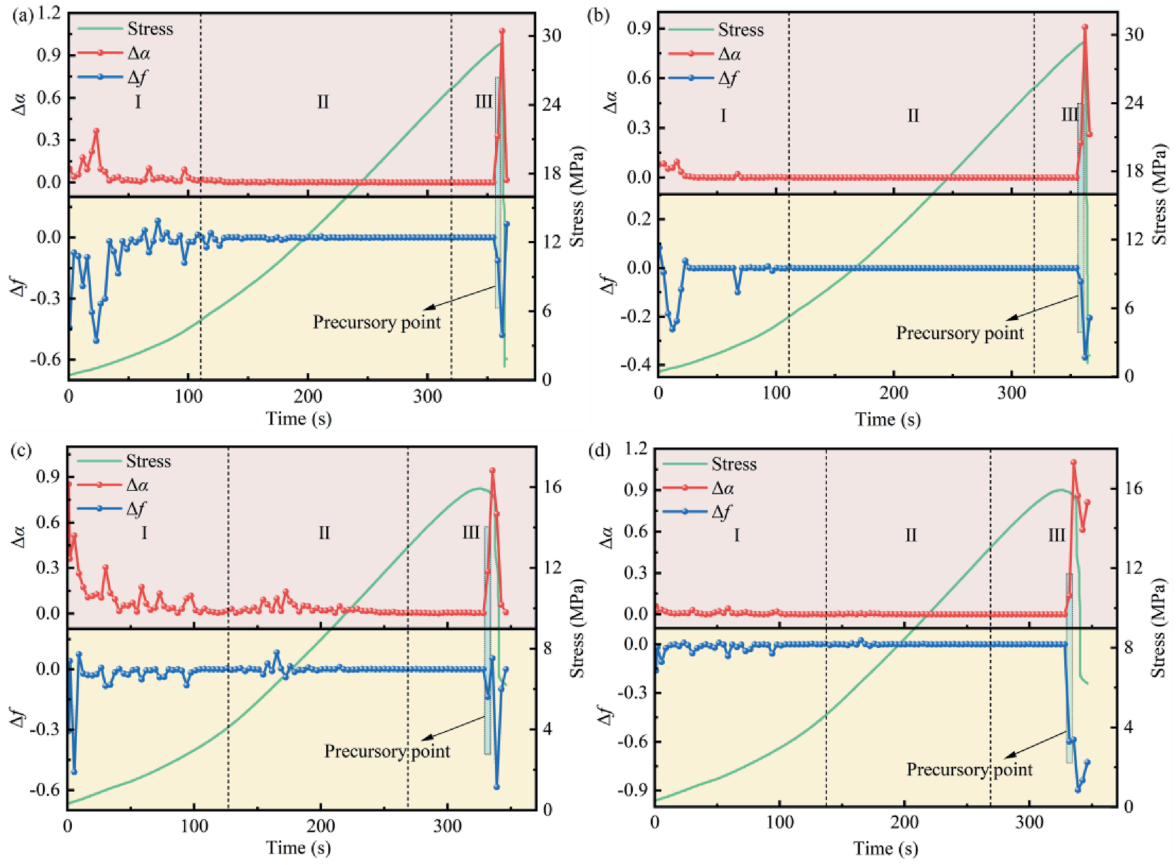

Fig. 15. Statistical results of multifractal spectra of EPs during failure: (a) Rock of RC-A-8, (b) Coal of RC-A-8, (c) Rock of RC-H-15, and (d) Coal of RC-H-15.

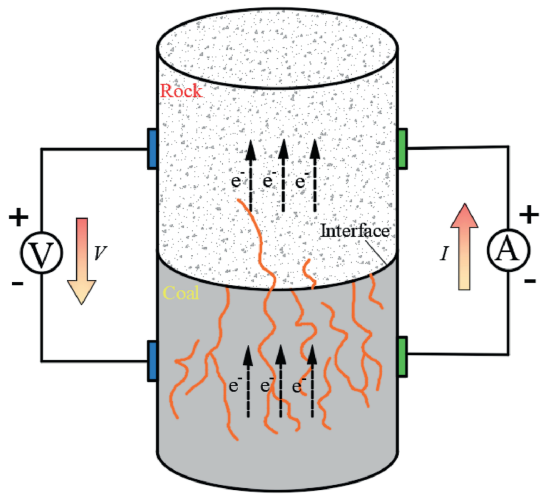

Fig. 16. Direction diagram of potential differences and weak currents within combined coal-rock (modified from Shan et al. (2024a)).

coal-rock interface identification and structural health monitoring, as shown in Fig. 9, achieving promising results. In addition, due to the timeliness and high sensitivity of EPs, they can quickly assess the depth, morphology, and stability of the coal-rock interface. The principle of coal-rock interface detection using EPs is based on the significant differences in the electrical conductivity between coal and rock layers, enabling the identification of stress states and deformation characteristics of different strata. In Section 3.2 and in reference to Shan et al. (2024a), the flow directions of potential differences (V) and weak currents (I) within combined coal-rock are illustrated in Fig. 16. It is concluded that the charges within the combined coal-rock move upward in a whole, with the measured weak currents flowing from the electrode on the coal to that on the rock, while the potential difference has the opposite direction.

To implement the EP method in an engineering field, it is crucial to reasonably design the electrode placement and electrode grid configuration according to the spatial arrangement of coal and rock layers. Typically, dedicated EP logging or through-layer boreholes are chosen as primary testing locations in coal mines. Common electrodes are placed on stable ground or in tunnels, while test electrodes are spaced evenly in a grid pattern along the borehole or logging wall. The electrode arrangement can be distributed both vertically and horizontally across different coal and rock layers, ensuring EP monitoring across entire areas and minimizing local interference. The EPs captured by the test electrodes are transmitted to the signal processing system in real time, which processes and stores the data. Based on the EPs collected from all electrode measurement points and their spatial coordinates, interpolation and inversion methods are employed to generate real-time EP spatial distribution model diagrams. Furthermore, the lower EP intensity bands observed at the coal-rock interface are used for interface identification. In addition, the appearance of abnormally high EP accumulation regions indicates that the rock mass in the localized area may have experienced fracture instability, indicating the need for prompt prevention and mitigation measures for potential coal-rock dynamic disasters. Moreover, as a nondestructive and noncontact

monitoring technique, the EP method can continuously monitor the stress distribution and deformation characteristics in composite coal-rock layers, providing early warnings for coal-rock dynamic disasters. This study employs a multifractal spectrum based on EPs to analyze the failure properties of composite coal-rock, and effective precursory information, as shown in Fig. 15. These findings indicate that the multifractal statistical features of EPs can serve as an important method for predicting coal-rock dynamic disasters.

In addition, the coal-rock interface used in this study is relatively smooth, representing a small-scale simplification and assumption of the actual interface at the site. However, the morphology and roughness properties of coal-rock interfaces are complex and variable in real coal mines, making the use of the EP method for interface orientation identification and fracture state characterization more challenging. Therefore, further experiments should be conducted on coal-rock combined samples under different interface morphology and roughness conditions, and rock samples containing natural coal-rock interfaces from mines can be used for testing.

Furthermore, the application of the EP method in the field faces challenges due to various factors, such as environmental conditions and equipment limitations. In complex mining environments, environmental electrical noise, gases, and mechanical interference can significantly impact the EP quality recorded. Therefore, the development of EP acquisition equipment and electrode systems with excellent anti-interference capabilities is crucial. Moreover, combining EPs with other geophysical signals, such as ultrasonic and micro seismic data, enhances the accuracy and reliability of coal-rock interface identification. Moreover, potential disasters such as water inrush and coal and gas outbursts are common in mines. Further research is needed to investigate the impacts of high temperature, water saturation and gas presence on the EP response characteristics of composite coal-rock failure.

5. Conclusions

In this study, uniaxial compression experiments were conducted on fine sandstone-coal and coarse sandstone-coal combined samples to monitor the EP response features during failure. The EP distribution contour maps and 3D EP spatial models were utilized to accurately identify the state of coal-rock interface. Furthermore, the relationships between the force chain fields and energy dissipation patterns obtained from numerical simulations and the EP response were explored. The multifractal characteristics of EPs were used to identify precursory information. The main conclusions can be summarized as follows:

(1) During the failure processes of combined coal-rock samples, the EP responses in both coal and rock strongly correlate with changes in the stress state, indicating significantly opposite polarities. The EPs exhibit minimal variation during the early loading stage, but begin to accelerate during the plastic stage. When the main failure occurs, the EPs experience instantaneous and significant fluctuations. The progressive failure processes of the fine sandstone-coal and coarse sandstone-coal combined samples differ notably, with the coal consistently experiencing more severe damage. In addition, the linear rebound phenomenon observed in fine sandstone leads to fluctuations in the EP response.

(2) The 2D EP distribution contour maps and 3D EP spatial models provide clear identification of the coal-rock interface and the damage states of samples. Before failure, the EP contour lines exhibit an approximately uniform distribution. The EPs in both the rock and coal gradually increase, while the green low-strength band at the interface remains parallel to the interface and at a low EP level. When failure occurs, the surface EP distribution of the samples is no longer balanced, and the green low-strength signal band at the coal-rock interface is not parallel to the interface, but instead crosses into the coal or rock, indicating structural failure of the sample.

(3) The EP responses of the combined samples are closely associated with the changes in the internal force chain field and the energy dissipation process. Numerical simulations of crack propagation in the two types of combined samples align well with the 3D EP spatial models and AE localization results. The regions with localized fractures, particularly at crack tips, tend to form sparse strong force chain fields, which can accumulate a large amount of charges under the influence of dislocation effects, leading to changes in EP responses. For fine sandstone-coal combined samples, sparse force chain fields predominantly appear within the coal, resulting in a significant increase in the EP level of the coal alone. For coarse sandstone-coal combined samples, the EP level increases significantly in both the coal and rock, primarily because the sparse force chain fields are concentrated within them. The evolution of the cumulative EP value is highly consistent with energy dissipation and can effectively characterize the energy transformation within the combined samples.

(4) The EPs of coal-rock combined samples exhibit multifractal characteristics during loading, satisfying scale invariance. The evolution of $\Delta\alpha$ and Δf can be divided into three stages, with their abnormal increases prior to sample failure serving as precursory indicators of impending failure. The relative magnitudes of $\Delta\alpha$ and Δf for coal and rock are closely related to their degree of damage. For the fine sandstone-coal combined samples, the coal exhibits larger $\Delta\alpha$ and smaller Δf than those of the rock, due to the less damage to the rock. For the coarse sandstone-coal combined samples, the differences in $\Delta\alpha$ and Δf between the coal and rock are not significant, as both experience severe damage.

This study reveals the failure behaviors and EP response features of combined coal-rock samples under uniaxial compression, exploring coal-rock interface identification and failure prediction for coal-rock composites through the EP method. Based on the EP test results under uniaxial compression, this paper discusses the effectiveness of applying the EP method to the study of failure monitoring in coal-rock composites. However, the morphology and roughness properties of coal-rock interfaces on site are complex and variable, indicating that simulated smooth coal-rock interfaces may be idealized. Therefore, future studies should consider combined coal-rock samples with varying interface morphologies and roughness, or even directly obtain rock blocks from coal mines in their natural state with coal-rock interfaces, to accurately characterize the stress states and locations of coal-rock interfaces using the EP method.

CRediT authorship contribution statement

Tiancheng Shan: Writing – original draft, Visualization, Supervision, Software, Methodology, Conceptualization. **Zhonghui Li:** Writing – review & editing, Supervision, Resources, Data curation, Conceptualization. **Enyuan Wang:** Writing – review & editing, Investigation. **Haishan Jia:** Supervision, Software. **Xin Zhang:** Supervision, Formal analysis. **Qiming Zhang:** Visualization. **Xiaoran Wang:** Writing – review & editing, Investigation. **Yue Niu:** Validation. **Shishi Deng:** Supervision.

Declaration of competing interest

The authors declare that they have no known competing financial interests or personal relationships that could have appeared to influence the work reported in this paper.

Acknowledgments

This research was supported by the National Natural Science Foundation of China (Grant No. 52574290), the National Key R&D Program of China (Grant No. 2022YFC3004705), and the Postgraduate Research & Practice Innovation Program of Jiangsu Province, China (Grant No. KYCX24_2913).

References

Archer, J.W., Dobbs, M.R., Aydin, A., Reeves, H.J., Prance, R.J., 2016. Measurement and correlation of acoustic emissions and pressure stimulated voltages in rock using an electric potential sensor. Int. J. Rock Mech. Min. Sci. 89, 26–33.

Aydin, A., Prance, R.J., Prance, H., Harland, C.J., 2009. Observation of pressure stimulated voltages in rocks using an electric potential sensor. Appl. Phys. Lett. 95, 124102.

Bai, L., Huo, Z., Zeng, Z., Liu, H., Tan, J., Wang, T., 2021. Groundwater flow monitoring using time-lapse electrical resistivity and self potential data. J. Appl. Geophys. 193, 104411.

Cai, R., Pan, Y., Xiao, Y., Liu, F., 2024. Study on loading rate and rock-coal strength ratio effect on mechanical properties of coal-rock combination. J. Min. Sci. 60, 196–209.

Cheng, Z., Li, L., Zhang, Y., 2020a. Laboratory investigation of the mechanical properties of coal-rock combined body. Bull. Eng. Geol. Environ. 79, 1947–1958.

Cheng, G., Bo, J., Ming, L., Li, F., Xu, S., 2020b. Quantitative characterization of fracture structure in coal based on image processing and multifractal theory. Int. J. Coal Geol. 228, 103566.

Dong, L., Tao, Q., Hu, Q., Deng, S., Chen, Y., Luo, Q., Zhang, X., 2022. Acoustic emission source location method and experimental verification for structures containing unknown empty areas. Int. J. Min. Sci. Technol. 32 (3), 487–497.

Eccles, D., Sammonds, P.R., Clint, O.C., 2005. Laboratory studies of electrical potential during rock failure. Int. J. Rock Mech. Min. Sci. 42 (7–8), 933–949.

Farhangi, V., Zadehmohamad, M., Monshizadegan, A., Izadifar, M., Moradi, M.J., Dabiri, H., 2023. Effects of geogrid reinforcement on the backfill of integral bridge abutments. Buildings 13 (4), 853.

Farhangi, V., Moradi, M.J., Daneshvar, K., Hajiloo, H., 2024. Application of artificial intelligence in predicting the residual mechanical properties of fiber reinforced concrete (FRC) after high temperatures. Constr. Build. Mater. 411, 134609.

Freund, F.T., Kulahci, I.G., Cyr, G., Li, J., Winnick, M., Tregloan-Reed, J., Freund, M.M., 2009. Air ionization at rock surfaces and pre-earthquake signals. J. Atmos. Sol. Terr. Phys. 71 (17–18), 1824–1834.

Fu, J., Haeri, H., Sarfarazi, V., Asgari, K., Marji, M.F., 2022. The shear behaviors of concrete-gypsum specimens containing double edge cracks under four-point loading conditions. Theor. Appl. Fract. Mech. 119, 103361.

Fu, J., Haeri, H., Labuz, J.F., Sarfarazi, V., Ebneabbasi, P., Aliha, M., Karimi, H.R., Jahanmiri, S., Marji, M.F., 2024. Determination of mode I fracture toughness of brittle materials with a new method. Acta Mech. Sin. 40 (2), 423236.

Haeri, H., Sarfarazi, V., Zhu, Z., Marji, M.F., Masoumi, A.R., 2019. Investigation of shear behavior of soil-concrete interface. Smart Struct. Syst. 23 (1), 81–90.

He, M., Ren, F., Liu, D., 2018. Rockburst mechanism research and its control. Int. J. Min. Sci. Technol. 28 (5), 829–837.

Higuchi, T., 1988. Approach to an irregular time series on the basis. Phys. D. 31 (2), 277–283.

Hu, S., Wang, E., Li, Z., Shen, R., Liu, J., 2014. Time-varying multifractal characteristics and formation mechanism of loaded coal electromagnetic radiation. Rock Mech. Rock. Eng 47, 1821–1838.

Huang, B., Liu, J., 2013. The effect of loading rate on the behavior of samples composed of coal and rock. Int. J. Rock Mech. Min. Sci. 61, 23–30.

Jiang, B., Wu, K., Wang, Q., Kang, H., Zhang, B., Zhang, Z., Chen, C., 2024. Development of physical model test system for fault-slip induced rockburst in underground coal mining. J. Rock Mech. Geotech. Eng. 17 (4), 2227–2238.

Jing, S., Wen, Z., Jiang, Y., Wen, J., Du, W., 2024. Mechanical behaviors and failure characteristics of coal-rock combination under quasi-static and dynamic disturbance loading: a case based on a new equipment. Geomech Geophys Geo 10 (1), 2.

Li, B., Wang, E., Li, Z., Cao, X., Liu, X., Zhang, M., 2023. Automatic recognition of effective and interference signals based on machine learning: a case study of acoustic emission and electromagnetic radiation. Int. J. Rock Mech. Min. Sci. 170, 105505.

Li, F., Yin, D., Wang, F., Jiang, N., Li, X., 2022. Effects of combination mode on mechanical properties of bi-material samples consisting of rock and coal. J. Mater. Res. Technol. 19, 2156–2170.

Li, L., Hu, X., Pan, Y., Sun, Y., 2024a. Experimental study on ultralow friction effect and acoustic emission characteristics of coal-rock interface with different roughness. Chin. J. Theor. Appl. Mech. 56 (4), 1047–1056.

Liu, X., Tan, Y., Ning, J., Lu, Y., Gu, Q., 2018. Mechanical properties and damage constitutive model of coal in coal-rock combined body. Int. J. Rock Mech. Min. Sci. 110, 140–150.

Liu, X., Liu, Z., Li, X., Gong, F., Du, K., 2020. Experimental study on the effect of strain rate on rock acoustic emission characteristics. Int. J. Rock Mech. Min. Sci. 133, 104420.

Li, Z., Zhang, X., Wei, Y., Ali, M., 2021. Experimental study of electric potential response characteristics of different lithological samples subject to uniaxial loading. Rock Mech. Rock. Eng 54, 397–408.

Li, Z., Shan, T., Wang, E., Niu, Y., Wang, X., Zhang, X., Jia, H., Chen, D., Yin, S., Sun, W., 2024b. Experimental study on response and precursor of pressure stimulated currents of combined coal-rock under cycling stress. Int. J. Rock Mech. Min. Sci. 177, 105745.

Lu, J., Jiang, W., Xie, H., Gao, H., Zhang, D., 2025. Dynamic disaster mechanism and acoustic emission evolution of deep coal-rock under true triaxial disturbance stress. J. Rock Mech. Geotech. Eng.

Ma, S., Liu, K., Guo, T., Yang, J., Li, X., Yan, Z., 2022. Experimental and numerical investigation on the mechanical characteristics and failure mechanism of cracked coal & rock-like combined sample under uniaxial compression. Theor. Appl. Fract. Mech. 122, 103583.

Purcell, E.M., Morin, D.J., 2013. Electricity and Magnetism, third ed. Cambridge University Press, Cambridge, pp. 261–262. 54(5).

Qiu, L., Song, D., He, X., Wang, E., Li, Z., Yin, S., Wei, M., Liu, Y., 2020. Multifractal of electromagnetic waveform and spectrum about coal rock samples subjected to uniaxial compression. Fractals 28 (4), 2050061.

Rutqvist, J., Birkhqlzer, J.T., Tsang, C., 2008. Coupled reservoir-geomechanical analysis of the potential for tensile and shear failure associated with CO_2 injection in multilayered reservoir-caprock systems. Int. J. Rock Mech. Min. Sci. 45 (2), 132–143.

Shan, T., Li, Z., Zhang, X., Jia, H., Wang, X., Wang, E., Niu, Y., Chen, D., Sun, W., Wang, D., 2024a. Pressure stimulated current in progressive failure process of combined coal-rock under uniaxial compression: response and mechanism. Int. J. Min. Sci. Technol. 34 (2), 227–243.

Shan, T., Li, Z., Jia, H., Wang, E., Wang, X., Niu, Y., Zhang, X., Chen, D., Yin, S., Zhang, Q., 2024b. Failure evolution and disaster prediction of rock under uniaxial compression based on non-extensive statistical analysis of electric potential. Int. J. Min. Sci. Technol. 34 (7), 975–993.

Song, H., Zuo, J., Liu, H., Zuo, S., 2021. The strength characteristics and progressive failure mechanism of soft rock-coal combination samples with consideration given to interface effects. Int. J. Rock Mech. Min. Sci. 138, 104593.

Shams, G., Rivard, P., Moradian, O., 2024. Tensile strength and failure behavior of rock-mortar interfaces: direct and indirect measurements. J. Rock Mech. Geotech. Eng. 16 (1), 41–55.

Stone, R.C., Farhangi, V., Fatahi, B., Karakouzian, M., 2023. A novel short pile foundation system bonded to highly cemented layers for settlement control. Can. Geotech. J. 60 (9), 1332–1351.

Triantis, D., Stavrakas, I., Anastasiadis, C., Kyriazopoulos, A., Vallianatos, F., 2006. An analysis of pressure stimulated currents (PSC), in marble samples under mechanical stress. J. Atmos. Sol. Terr. Phys. 31 (4–9), 234–239.

Vallianatos, F., Tzanis, A., 1998. Electric current generation associated with the deformation rate of a solid: preseismic and coseismic signals. Phys. Chem. Earth 23 (9–10), 933–938.

Vallianatos, F., Triantis, D., Tzanis, A., Anastasiadis, C., Stavrakas, I., 2004. Electric earthquake precursors: from laboratory results to field observations. Phys. Chem. Earth 29 (4–9), 339–351.

Varotsos, P.A., Sarlis, N.V., Skordas, E.S., 2002. Long-range correlations in the electric signals that precede rupture. Phys. Rev. E. 66 (1), 011902.

Wang, X., Shan, T., Liu, S., Li, Z., Liu, X., Wang, E., Li, N., Wang, J., 2024. Thermal-damage effects on fracturing evolution of granite under compression-shear loading. Theor. Appl. Fract. Mech. 133, 104581.

Wang, J., Chen, G., Xu, Q., 2024. Seismic signal characteristics and precursory information of bedding landslide with locked segments. Eng. Geol. 341, 107709.

Wang, J., Feng, K., Wang, Y., Lin, G., He, C., 2022. Soil disturbance induced by EPB shield tunnelling in multilayered ground with soft sand lying on hard rock: a model test and DEM study. Tunn. Undergr. Space Technol. 130, 104738.

Xiao, X., Ding, X., Zhao, X., Pan, Y., Wang, A., Wang, L., 2017. Experimental study on acoustic emission and charge signals during coal failure process at different loading rates. Rock. Soil. Mech. 38 (12), 3419–3426.

Xie, H., Gao, M., Zhang, R., Peng, G., Wang, W., Li, A., 2019. Study on the mechanical properties and mechanical response of coal mining at 1000 m or deeper. Rock Mech. Rock. Eng 52, 1475–1490.

Xu, C., Yang, T., Wang, K., Yuan, Y., Guo, L., 2024. Influence of primary interface characteristics on mechanical properties and damage evolution of coal-rock combination. Eng. Fail. Anal. 164, 108658.

Yao, Q., Wang, W., Zhu, L., Xia, Z., Tang, C., Wang, X., 2020. Effects of moisture conditions on mechanical properties and AE and IR characteristics in coal-rock combinations. Arabian J. Geosci. 13, 1–15.

Yang, E., Li, S., Lin, H., Zhao, P., Qin, L., Zhao, B., 2022. Influence mechanism of coal thickness effect on strength and failure mode of coal-rock combination under uniaxial compression. Environ. Earth Sci. 81 (17), 429.

Yi, X., Wang, L., Liu, J., Ranjith, P.G., Gao, F., Cai, C., Xie, H., 2024. Experimental study on the effect of heating and liquid nitrogen-cooling cyclic treatment on mechanical properties and fracturing characteristics of granite. Int. J. Rock Mech. Min. Sci. 176, 105691.

Yoshida, S., Ogawa, T., 2004. Electromagnetic emissions from dry and wet granite associated with acoustic emissions. J. Geophys. Res. Solid Earth 109 (B9), B9204.
Zhang, H., Lu, C., Liu, B., Liu, Y., Zhang, N., Wang, H., 2020. Numerical investigation on crack development and energy evolution of stressed coal-rock combination. Int. J. Rock Mech. Min. Sci. 133, 104417.
Zhao, Z., Wang, W., Wang, L., Dai, C., 2015. Compression-shear strength criterion of coal–rock combination model considering interface effect. Tunn. Undergr. Sp. Tech. 47, 193–199.
Zuo, J., Wang, Z., Zhou, H., Pei, J., Liu, J., 2013. Failure behavior of a rock-coal-rock combined body with a weak coal interlayer. Int. J. Min. Sci. Technol. 23 (6), 907–912.

Zhonghui Li is a professor in the School of Safety Engineering, China University of Mining and Technology. He obtained his PhD in Safety Science and Engineering from China University of Mining and Technology in 2007 and was awarded the National Excellent Doctoral Dissertation Award. His research mainly focuses on the intelligent monitoring and early warning of coal-rock dynamic disasters, especially the prevention of coal and gas outbursts and geophysical responses. He has led more than 10 national-level high-profile projects supported by the National Natural Science Foundation of China and National Key R&D Program of China, and has published over 50 SCI papers in prestigious journals. He serves as an editorial board member of four Chinese journals. He has guided his postgraduate students to obtain one Jiangsu Provincial Excellent Doctoral Thesis award and three Jiangsu Provincial Excellent Master's Thesis awards.